Research Article Vol. 1, No. 7 / 15 Jul 2022 / Optics Continuum 1529
OPTICS CONTINUUM

Elliptical plasmonic near-field transducer and v-shape waveguide designs for heat assisted magnetic recording

MUGAHID ALI,[1,4] FRANK BELLO,[1] NICOLÁS ABADÍA,[2] FUMIN HUANG,[3] AND JOHN DONEGAN[1,5]

[1] School of Physics, CRANN, and AMBER, Trinity College, Dublin 2, Ireland
[2] School of Physics and Astronomy and Institute for Compound Semiconductors, Cardiff University, Cardiff CF24 3AA, UK
[3] School of Mathematics and Physics, Queens University Belfast, Belfast, BT7 1NN, UK
[4] alim2@tcd.ie
[5] jdonegan@tcd.ie

Abstract: We proposed a new elliptical near-field transducer (NFT) and V-shaped waveguide design, which provides multiple pathways to control and optimise the thermal performance of the optical delivery paths for heat-assisted magnetic recording (HAMR). The principle of operation of the design utilises the properties of the localised surface plasmon resonance (LSPR) of the metallic elliptical NFT. We demonstrated a peak temperature in the recording media normalised to the incident laser power (T_{Media}/P_{In}) ranging from ~ 128 K/mW to more than 181 K/mW. We also achieved tunable thermal gradients as high as 23.0 K/nm and 18.7 K/nm in the recording media's down-track and cross-track directions, respectively. Moreover, we exemplified that the inevitable temperature rise in the plasmonic NFT could be tuned to remain under 400 K for maximum heat in the recording media > 700 K. The best thermal performance obtained corresponded to the aspect ratio of the antenna a/b ~ 0.89 with the minor axis of the antenna $a = 85$ nm.

1. Introduction

Plasmonic devices have received a great deal of attention in the past decades due to their ability to concentrate electromagnetic radiation to sub-diffraction limited spots on the order of a few nanometres while enhancing the field intensity by a few orders of magnitudes [1,2]. These remarkable properties have facilitated the development of a wide range of technologies, including near-field optical microscopy, photodynamic therapy, plasmonic biosensors, and subwavelength waveguides, to name just a few. However, the use of plasmonic systems for high-temperature applications remains mired by the limitations of plasmonic materials, which are mainly due to losses at optical frequencies [3]. These have become an urgent bottleneck issue holding back the commercialisation of many plasmonic technologies, particularly heat-assisted magnetic recording (HAMR) in data storage [4,5]. Moreover, it set significant barriers restricting fundamental nanoscale research in a high-temperature environment, such as solar thermophotovoltaics and the burgeoning studies of nanoscale thermodynamics that are fundamental to nanochemistry.

HAMR is a method for encoding information in magnetic media with nanoscale track widths (< 50 nm) to enable high areal densities (ADs) beyond 2 Tb/in^2 in the recording medium of next-generation hard disk drives (HDD) [6]. In this technique, the light from a laser (typically at λ = 830 nm) is guided in an optical waveguide and coupled either evanescently [7] or by direct-fire approach [8] to an aperture-, or apertureless-based plasmonic antenna (near field transducer

#460036 https://doi.org/10.1364/OPTCON.460036
Journal © 2022 Received 26 Apr 2022; revised 9 Jun 2022; accepted 13 Jun 2022; published 28 Jun 2022

OPTICS CONTINUUM

(NFT)) attached to its end. It is designed to focus the electromagnetic power into an area smaller than 50×50 nm^2 in a high coercivity material to heat it to above its Curie temperature ($\backsim$750 K for bulk L_{10} FePt) [9]. A range of such devices has been investigated, including C-, E-, and H-shaped apertures [10–12], bow-tie apertures [13,14], triangular antenna [15], lollipop antenna [4], droplet antenna [16], and the nanobeak antenna [17].

In such applications, beyond the temperature magnitude, the in-plane temperature distribution (i.e., thermal gradient) of the sub-nanometre confined thermal energy is a crucial parameter that needs to be considered. In addition, the heat transfer process makes obtaining a sizeable thermal gradient on a nanoscale region challenging. Furthermore, plasmonic applications have different requirements regarding this metric, which depend on the material and the design of the plasmonic system. For instance, in array-based nano-reactors for plasmonic photocatalysis, a thermal gradient of 1.9 K/nm is obtained [18]. In comparison, values as high as 15 K/nm have been reported for antenna-based plasmonic near-field transducers used in HAMR applications [19], the focus of this work.

The nanofocusing of electromagnetic energy in HAMR applications can be attained straightforwardly using the localised surface plasmon resonances (LSPR) [20] supported by the plasmonic device in use. However, the challenging aspect of this nanofocusing process is the thermal management of the system, for instance, (i) the thermal efficiency of the system, which measures the peak temperature in the media relative to the peak temperature in the NFT for a given incident laser power. This metric should be as large as possible since the largest increase in media temperature for the smallest increase in NFT temperature is desired to prevent the NFT from getting too hot; otherwise, the NFT could deform or melt, degrading its performance. The highest value for this metric was 8.60, obtained in a numerical study using an NFT of an alloy of $Au_{0.175}Ag_{0.875}$ for a laser power of 4.9 mW [19], (ii) the thermal spot profile in the media at the full width at half maximum (FWHM) should maintain its 'squareness' to avoid having a long thermal tail in the media in both the cross-track and down-track directions, (iii) the thermal gradient in the media, which must be as large as possible, as having a sharp thermal gradient allows writing sharp transitions that are key to high linear densities, (iv) the normalised peak temperature, which measures the peak temperature in the media normalised by the total power incident on the NFT must also be as large as possible; it determines how much laser power is needed to deliver to excite the NFT and is also helpful for characterising the effects of laser intensity noise on the recording system [21], (v) and indeed the most problematic and central to all the aforementioned requirements is the reliability of the plasmonic near-field transducer itself, which is generally made of gold and must withstand the inevitable high temperature within the HAMR system.

Advantageously, in most high-temperature plasmonic applications, including HAMR, the plasmonic nanostructure in question does not have to be at a specific temperature but rather should be illuminated until a specific optical output is reached [22]. For instance, the use of alternative plasmonic materials that have very high melting points, like titanium nitride, zirconium nitride, tungsten, etc. [23,24], is not necessarily the best option for making better plasmonic NFTs for high-temperature applications. As these materials have high optical absorption and require much more incident power in order to produce the same strong near-field enhancement that is produced by noble plasmonic materials like gold or silver. This causes a significant self-heating effect [25] in these materials, which severely affect the performance of nearby devices in the system, such as the write pole in the case of HAMR, hence, affecting the thermal performance of the whole system. To a large extent, this means that we could alleviate the self-heating burden and side-step the limitations of using noble plasmonic materials for high-temperature applications via engineering the architecture of the plasmonic nanostructures and the optical delivery path to optimise the optical output and the near-field enhancement.

OPTICS CONTINUUM

A "wired" configuration, in which a surface plasmon polariton (SPP) is excited and propagated along a plasmonic waveguide of many micrometres long ($\backsim$ 6 μm), achieved a thermal efficiency of 5.91% in [26]; outperforming other contending optical antenna designs (Lollipop and C-aperture) used for HAMR. Furthermore, the long tapered structure is also found to be most efficient for converting the plasmonic mode in the NFT to thermal energy in the recording media, even without optimisation [22], as it can efficiently match its radiation resistance impedance (*a quantity that depends on the length of the antenna*) to the impedance of the recording medium [8]. On the other hand, "wireless" configurations have demonstrated outstanding potential for managing the optical and thermal performance of the HAMR plasmonic systems. The plasmonic antennas are located far from the laser sources in such designs. The localised surface plasmons resonance (LSPR) is excited via an evanescent coupling approach for an antenna with a tapered structure [27] and via a direct-coupling method in a design that uses a metal-insulator-metals (MIM) configuration and reflection coatings in the waveguide [19].

This work proposes a novel design of an optical delivery system consisting of an elliptical plasmonic antenna (NFT) and a V-shaped waveguide. We adopt the "wireless" configuration where the light from the laser is coupled evanescently to the NFT at the end of the V-shaped waveguide. The optical properties of the elliptical geometry and its usage in plasmonic applications have been investigated thoroughly in [4]. Here we study its use as a near-field transducer in an optical delivery path for HAMR. The geometrical parameters of the elliptical antenna provide means to control the near field enhancement and to support higher-order plasmonic modes, which help match its radiation resistance impedance to the impedance of the recording medium [8]. On the other hand, the V-shaped waveguide could also be controlled to optimise the light coupling to the elliptical plasmonic antenna for the chosen elliptical antenna parameters. The proposed system provides flexibility and several degrees of freedom to manage the optical and thermal performance of the HAMR optical delivery path and an optimal photonic-plasmonic-thermal conversion yield. The study was performed numerically using (COMSOL Multiphysics software) [28]. Maxwell's equations are initially solved to determine the power dissipated due to resistive losses in the computational region, which is then applied to the heat transport equations as a heat energy transfer rate. The software discretises and solves the coupled heat transport and electromagnetic equations on a finite-element mesh in three dimensions.

2. Results and discussion

The proposed optical delivery path consists of a V-shaped waveguide (Fig. 1(a)) that evanescently couples a photonic mode from a semiconductor laser to a plasmonic mode supported by an elliptical antenna (Fig. 1(b)) positioned 10 nm above the core at the end of the waveguide (Fig. 1(a) - insets (i) and (ii)). Each of the two arms of the waveguide is designed for single-mode excitation at a continuous wavelength of 830 nm. The injected modes are TE_{10}-modes, and they are 180$\circ$ out of phase to allow for the excitation of the quadrupole or higher-order modes based on the size of the plasmonic NFT. The angle φ between the arms of the waveguides was adjusted until maximum coupling to the plasmonic mode was achieved at $\varphi = 54^{\circ}$. It should be noted here that all the parameters of the design are tied together; for instance, changing the dimensions of the elliptical antenna changes the plasmonic mode supported and hence requires a new coupling configuration, which also requires a change of the waveguide angle φ.

The choices of waveguide materials for the magnetic head industry are limited since these materials must have long-term stability. The core of the waveguide usually is tantalum oxide (Ta_2O_5), and the cladding materials could be either aluminium oxide (Al_2O_3) or silicon dioxide (SiO_2) [29]. Recently, other materials such as silicon nitride (Si_3N_4) [19,30] and silicon (Si) [27] have also been investigated. The core material in the proposed design in this work is silicon (Si) fully embedded in silicon dioxide (SiO_2) cladding. The reason for this choice is the high refractive index of silicon which provides better light confinement and coupling to high

OPTICS CONTINUUM

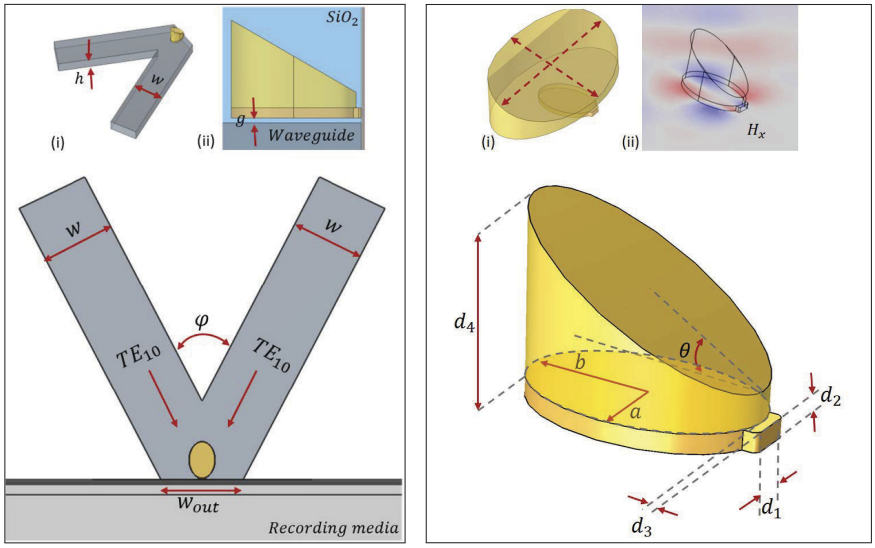

(a) V-shaped waveguide

(b) Elliptical antenna

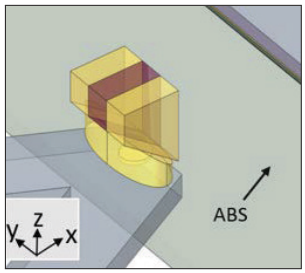

(c) 3D view

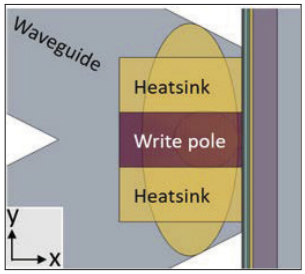

(d) Top view

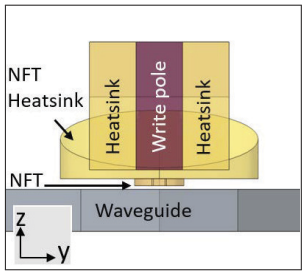

(e) ABS view

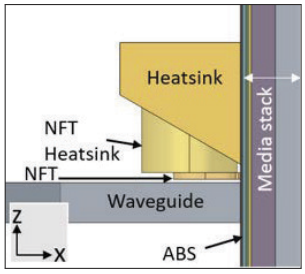

(f) Side view

Fig. 1. (a) is the V-shape waveguide design. w and h are the width and height of the waveguide arm, respectively, w_{out} is the width of the waveguide exit port, φ is the angle between the two arms. (b) is schematic of the proposed elliptical NFT. The dimensions a and b are the minor and major axes of the antenna, respectively. d_1 is the width of the tip, d_2 is the height of the main body of the antenna, d_3 is the extension of the tip from the body of the NFT, d_4 is the height of the back end of the antenna, and θ is the angle of the taper of the top section of the NFT which also acts as a heat sink. (c), (d), (e), and (f) are labelled schematics of the complete optical delivery path. The Initial dimensions and materials properties are listed in (Table 1). The Si-waveguide is cladded in SiO_2. ABS-air bearing surface.

OPTICS CONTINUUM

effective index plasmon modes. More importantly, the much higher thermal conductivity of Si (k = 130 W/(m.K)) compared to Ta_2O_5 (k = 0.45 W/(m.K)), which would help markedly lower the steady-state temperature of the NFT given equal amounts of dissipated power [27]. Notwithstanding, Silicon Nitride material, for example, could have been chosen in this work instead. In this case, the waveguide height (h) should be increased from 120 nm to 180 nm, and the gap (g) between the antenna and the waveguide should also increase from 10 nm to 188 nm for best evanescent coupling of the photonic mode in the waveguide to the plasmonic mode in the antenna as shown in a previous study [31]. Therefore, the flexibility of the design allows for various choices of materials and dimensions to be investigated.

The NFT used in the proposed optical delivery path for HAMR has elliptical geometry (Fig. 1(b)). All the dimensions shown in this diagram can be manipulated to optimise the performance of the antenna. a and b are the minor and major axes of the antenna, respectively. Tuning these two dimensions independently provide more control on the NFT performance than the conventional lollipop NFT. Varying the lengths a and b generate different charge distributions; consequently, different order plasmonic modes could be supported according to their resonance with the incident wavelength. This will have a significant influence on the thermal performance of the HAMR system.

The tip is designed with rounded corners with a radius of 5 nm to evade large field enhancement at perfectly sharp edges, which are not easy to make practically, for instance, because of the proximity effect [32], which limits the achieved resolution in electron-beam lithography in the nanofabrication process. Its width d_1 controls the cross-track length of the heated region in the recording medium. The height d_2 should be minimised to mitigate the propagation of the surface plasmon along the tip at the Air Bearing Surface (ABS) [27] (see Fig. 1((c) and (f)) and to reduce the down-track size of the hot spot. It should also be noted here that the surface plasmon in this design is generated at the bottom surface of the antenna at the interface between the plasmonic and the dielectric spacer layer (*the H_x component of the plasmonic mode is shown in Fig. 1(b) - inset (ii)*). However, the top part of the elliptical body (*the gold material present above the height d_2*) could be extended (Fig. 1(b) - inset (i)) to act as a heatsink for the NFT at no cost to the optical performance [27].

The gap between the antenna and the waveguide has a thickness g (Fig. 1(a) - inset (ii)) which is also important to match the photonic-plasmonic modes coupling [27,33]. d_3 and d_4 define the extension of the tip and the height of the back end of the antenna, respectively, which are also needed to optimise the coupling of power from the waveguide to the antenna and from the antenna to the recording medium. The angle θ is adjusted to keep the write pole away from the body of the antenna, so it does not interfere with the plasmon mode while maintaining a close distance of 30 nm of the tip in the front side to enable easy data encoding. Figures 1((c), 1(d), 1(e), and 1(f)) show a schematic of the complete optical delivery path proposed in this work. The various components are labelled on the diagram.

The dimensions of the tip d_1 and d_2 are set for the desired hot spot size in the recording media. The gap g is set to optimise the photonic mode coupling from the waveguide to the plasmonic mode of the NFT. d_3 is adjusted to optimise the confinement of the near-field and hence, the conversion process of the plasmonic mode to a hot spot in the recording media. d_4 is the height of the backside of the top part of the antenna, which acts as a heatsink. The minor and major axes dimensions of the antenna $a = b = 85$ nm that corresponds to the conventional circular shape of the antenna are the initial values that produced the maximum photonic to plasmonic coupling; then a is kept fixed while b varied during the study. Here, the role of the V-shaped design of the waveguide comes into play as it could easily modify the coupling arrangement for the guided photonic mode to the supported plasmonic mode based on the chosen parameters of the NFT. The chosen material for the elliptical NFT was gold for its superior plasmonic performance compared

OPTICS CONTINUUM

to other plasmonic materials [34]. An in-depth discussion of HAMR plasmonic materials can be found in [6].

2.1. Photonic→ plasmonic→ thermal conversion processes

The efficiency of the photonic → plasmonic → thermal conversion processes depends on the geometries and materials of the transducer, waveguide [6], and the dielectric spacer layer between them [33]. And it is also affected by the presence of any metal in proximity (e.g., write pole, heatsink, recording media, etc.). These processes are illustrated in (Fig. 2). First, the photonic TE_{10}-mode is launched and propagates on both sides of the waveguide arms with a π-phase shift to allow exciting a quadrupole or higher-order localised surface plasmon resonance (LSPR) mode, according to the size of the NFT [7]. We highlighted the magnetic field component, H_x of such a mode at the bottom surface of the antenna for an incident laser power of 7.25 mW; the same laser power that is used in the comparative study in section 2.3. The plasmonic mode concentrates the light at the tip due to the lightning rod effect [35]. Finally, the energy dissipates in the lossy magnetic material, creating the required hot spot where the dimensions of the tip determine its profile. The smaller the tip, the higher the system's ADC; however, the frailer the NFT would be, and a careful trade-off needs to be made.

The maximum temperature generated in the media was 932 K, achieved with an antenna with the tapered angle ($\theta = 30^\circ$) and a minor and major axes of sizes (a = 85 nm) and (b = 95 nm), respectively, as shown in Fig. 2. However, it is expected that increasing the size of the antenna, which is desired for fabrication tolerance, would require re-optimising all the other parameters in the design to optimise the photonic → plasmonic → thermal conversion processes.

2.2. Thermal behaviour of the system

Based on the structural, optical and thermal properties of the different devices and stack materials shown in Table 1, we analysed the thermal performance within the system. Figure 3(a) demonstrates the overall temperature profile within the different components. The maximum temperature recorded in a plane at the middle of the magnetic recording layer reached 932 K for a total laser power of 7.25 mW, indicating efficient heating. Figure 3(b) shows a close up of the generated hot spot concentrated within < 50 x 50 nm^2 in the FePt recording layer. Such an area meets industry standards of storage densities of 1 Tb/in^2 or larger. It is determined by and large by the dimensions of the elliptical antenna tip at the ABS and the thermal gradient magnitude within the media. The recording medium layer FePt has a $\backsim$ 750 (K) Curie temperature.

The necessary quantities for qualitative and quantitative analysis of the system's thermal behaviour are presented in Figs. 4(a–c). Figure 4(a) compares the maximum temperature in the media, NFT and the write pole as a function of the eccentricity of the NFT. While the temperature in the HAMR media needs to be maximised to above its Curie temperature, it needs to be minimised in the other components to ensure devices reliability and durability, the task that is demonstrated in section 2.3. But in general, the typical specification is that the electromagnet must be under $450K$ to avoid a substantial deterioration of the magnetic flux output from the write head [22]. On the other hand, the temperature of the NFT must remain under 400 K if it is made of gold, as it is known to become significantly malleable at this point.

The down-track and cross-tack thermal gradients of the hot spot are highly important too. These quantities must be above 10 K/nm for high areal densities and to not overwrite adjacent bits with parasitic heating [19]. The thermal gradient is strongly affected by multiple factors, including the shape of the antenna [18,36], the dimensions of the various layers in the recording film stack [22], and the power of the laser, to name a few. Figure 4(b) depicts the change of the down-track (black marks) and cross-track (red marks) thermal gradients, with maximum values of 23.2 K/nm and 17.7 K/nm, respectively, for the aspect ratio of the antenna $a/b \backsim 0.89$.

OPTICS CONTINUUM

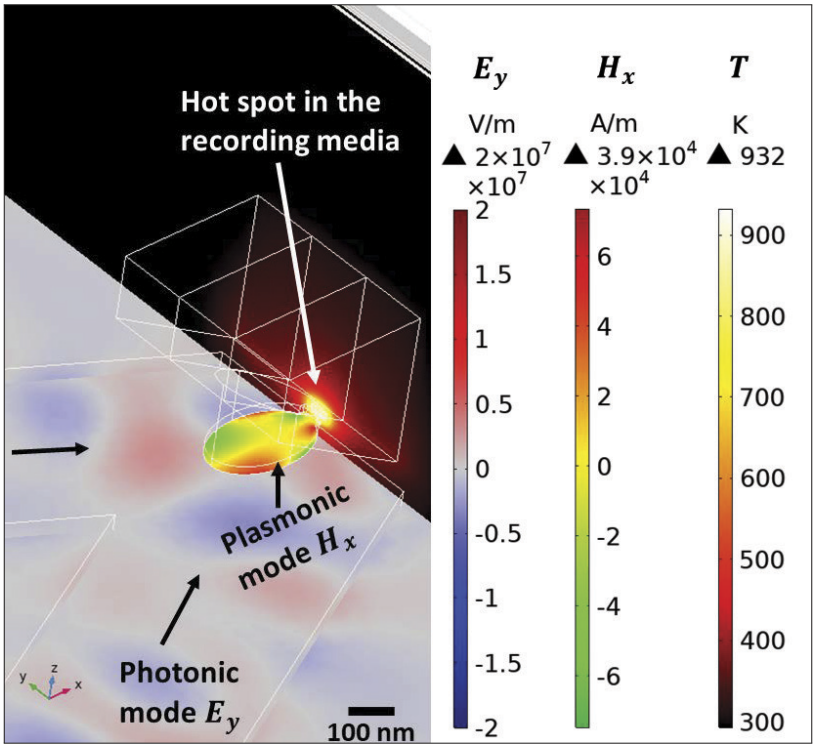

Fig. 2. The diagram demonstrates the coupling of photonic to plasmonic mode and the coupling of plasmonic to hot spot in the recording media. The TE_{10} guided mode in the waveguide, E_y, excites the antenna's localised surface plasmon resonance (LSPR) mode, the H_x component of which is plotted at the NFT-spacer layer interface, and which in turn concentrates the light and dissipates the energy in the lossy magnetic material creating the hot spot in the recording medium. Due to the tapered angle ($\theta = 30°$) and the size of the minor (a=85 nm) and major (b=95 nm) axes of the elliptical antenna, the tapered write pole is 216 nm high above the NFT-dielectric interface at the back-end of the NFT and 30 nm from its tip for easy data encoding. This arrangement prevents the write pole and heatsinks from affecting the photonic-plasmonic modes coupling.

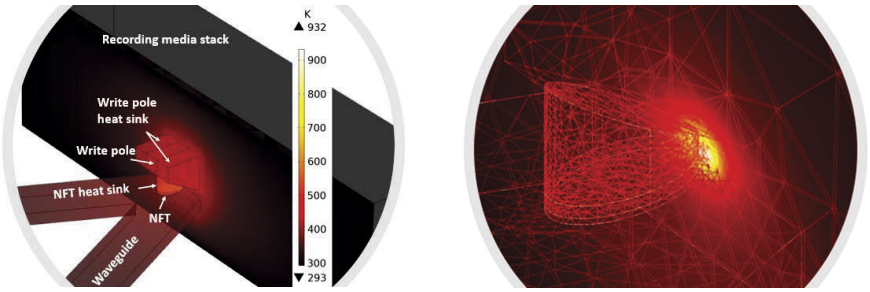

(a) (b)

Fig. 3. (a) is an overall view of the temperature distribution in the proposed HAMR optical delivery system elements, (b) a close-up of the hot spot in the media.

OPTICS CONTINUUM

Table 1. Structural, optical, and thermal properties in the proposed HAMR system. The values of the optical and thermal properties are obtained from [19].

Device	Dimensions	n	k	Heat Capacity ($J \cdot kg^{-1}K^{-1}$)	Thermal Conductivity ($W \cdot m^{-1}K^{-1}$)
Au NFT	b = variable, a = 85 nm, d_1 = 50 nm, d_2 = 20 nm, d_3 = 10 nm, d_4 = 196 nm, g = 10 nm, $\theta = 30°$	0.17	5.17	129	140
Au NFT Tip	50 nm (wide at ABS), 20 nm thick	0.17	5.17	129	140
Si Waveguide	w = 483 nm, h = 120 nm, w_{out} = 540 nm, $\varphi = 54°$	3.48	0.004	700	130
SiO_2 Cladding	-	1.4	0	703	1.25
CoFe Write Pole	160 (wide at ABS)	3	4	430	15
Air + Lubricant mixture	2 nm thick	2.9	0.12	1	1
Carbon Overcoat	2 nm thick	1.32	0.0021	1	3
Capping Layer	2.5 nm thick	2.22	0.17	1	1
FePt Recording Layer	10 nm thick	3.04	2.69	200	5.7, 1.14 in-plane
MgO Interlayer	7 nm thick	1.65	0	838	3
Amorphous Underlayer	9 nm thick	3.72	3.99	1750	10.5
Heatsink	72 nm thick	5.87	4.68	1050	70
Media substrate	Infinite	1.4	0	703	1.25

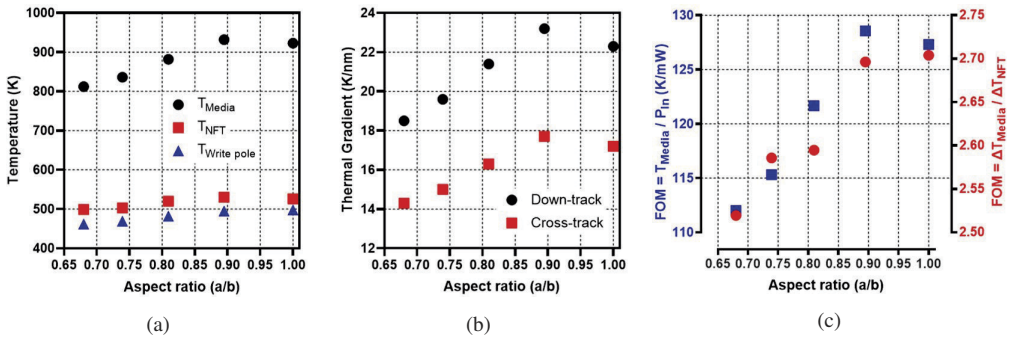

(a) (b) (c)

Fig. 4. The figures show the thermal performance as a function of the aspect ratio of the elliptical antenna. (a) is the highest temperature recorded in the different components, (b) thermal gradients, and (c) is the figures of merit recorded as a function of the aspect ratio of the elliptical antenna.

OPTICS CONTINUUM

Figure 4(c) shows the results for two figures of merits (FOMs) that quantify the system's thermal performance. The first is the thermal efficiency ($\Delta T_{Media}/\Delta T_{NFT}$) (red marks), which measures the peak temperature in the media relative to the peak temperature in the NFT for a given incident power. This metric should be as large as possible to achieve the largest increase in temperature in the recording media for the smallest increase in the temperature of the NFT. The other is the normalised peak temperature (T_{Media}/P_{In}) K/mW (blue marks) which measures the peak temperature in the media normalised by the incident laser power. It indicates how much laser power is needed to be delivered to the NFT for a specific output which is useful for characterising the effects of laser intensity noise on the recording system [21]. The curves in Figs. 4(a–c) demonstrate the tunability of the thermal performance with the aspect ratio of the elliptical antenna, which shows peaks at a ratio of $\backsim$0.89.

2.3. Comparison with other NFTs

Here, we perform comparative studies of the thermal behaviour of the proposed optical delivery path for HAMR featuring the elliptical antenna and the V-shaped waveguide with other near-field transducers designs. The studies compare conventional [36] and high-performance [19] designs. The thermal performance of a triangular antenna, E-antenna, and a lollipop antenna from [36] is plotted along that of the elliptical antenna (Fig. 5) with red, yellow, blue and green colours bars, respectively. All the antennas are excited with the same laser power of 5 mW, which is the power used in [36]. Here, the elliptical antenna has a major axis $b = 95\ nm$ and a minor axis $a = 85\ nm$. From a glance at the figures, the superiority of the elliptical antenna design performance is apparent. The figures of merits used here are the same as those discussed in the previous section.

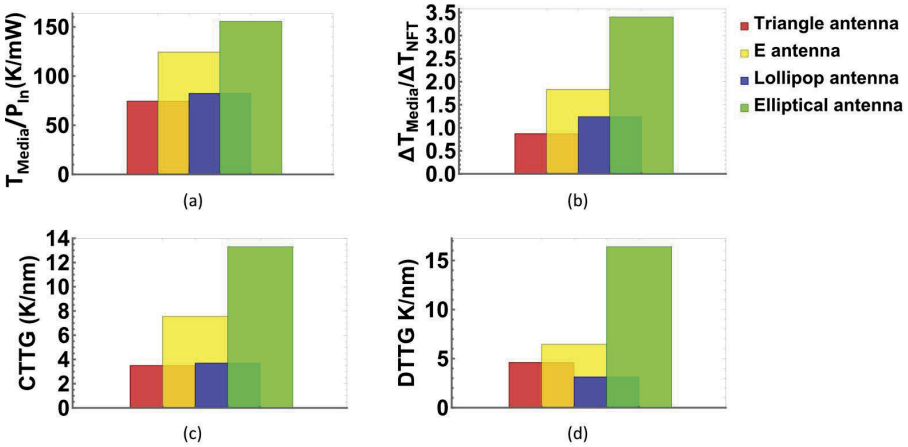

Fig. 5. The figures compare the thermal performance at the steady-state for various antenna designs reported in [36] with the elliptical antenna proposed in this work. (a) is the normalised peak temperature (T_{Media}/P_{In}) K/mW, (b) is the thermal efficiency ($\Delta T_{Media}/\Delta T_{NFT}$), (c) is the cross-track, and (d) is the down-track thermal gradients.

Figure 5(a) is the maximum temperature in the media normalised to the laser power, which indicates the efficiency of the photonic to plasmonic, and the plasmonic to thermal conversion processes. The elliptical antenna produced the highest normalise peak temperature with a value of $\backsim$ 150 K/mW. Figure 5(b) is the thermal efficiency ($\Delta T_{Media}/\Delta T_{NFT}$) which quantifies the ratio of the temperature rise in the media to the temperature rise in the NFT. The thermal efficiency of the elliptical antenna (green bar) is almost twice that of the best of the other three antennas (yellow bar). Figures 5(c) and 5(d) are the media's cross-track and down-track thermal gradients, respectively. The values presented here are greater than the other antennas in this comparative

OPTICS CONTINUUM

study and close to or even better than values obtained from different designs ([18,19,37–39]. It is also worth mentioning that the analysis in [36] did not ponder the presence of any nearby metallic components such as the write pole or heatsinks to the NFT, which would have undoubtedly affected the performance of these antennas.

The results of another comparison with the optical delivery path design using metal-insulator-metal (MIM) NFT design [19] is presented in (Table 2). This MIM design demonstrated a high standard of thermal performance and considered all the devices close to the NFT in the HAMR head.

Table 2. Comparison of the thermal performance of the elliptical NFT with MIM NFT design.

	$\frac{\Delta T_{Media}}{\Delta T_{NFT}}$	T_{NFT}	T_{Media}	Down-Track Gradient	Cross Track Gradient
			$P_{In} = 7.25\ mW$		
MIM NFT [19]	5.25	394 K	823 K	14.4 K/nm	11.8 K/nm
Elliptical Antenna Design (1)	3.38	495 K	976 K	23.0 K/nm	18.7 K/nm
			$P_{In} = 3.9\ mW$		
Elliptical Antenna Design (2)	4.09	394 K	706 K	14.2 K/nm	11.3 K/nm

The elliptical antenna design (1) compared the case in Ref. [19] for the incident laser power of $P_{In} = 7.25\ mW$, where we used similar optical and thermal properties of the materials in the simulations with slight changes in the thicknesses of a few layers in the recording media stack (Table 1). The best performance in each metric is highlighted in green. The elliptical antenna resulted in significantly improved values of 23.0 K/nm and 18.7 K/nm for both the down-track and the cross-track thermal gradients, respectively, and in higher temperature rise in the recording media per milli-watt of laser power $T_{Media}/P_{In} \sim 134$ K/mW. However, the temperature of the NFT increased significantly to 495 K. This is an unwanted result for the HAMR application, where the NFT has to remain under 400 K if it is made of gold, as discussed previously. Notwithstanding, the temperature of the NFT and the metric $(\Delta T_{Media}/\Delta T_{NFT})$ for the elliptical antenna could be improved, for instance, by reducing the power of the laser, by changing the aspect ratio of the antenna, or by varying any of the parameters shown in Fig. 1. We showed improved performance in the elliptical antenna design (2) by reducing the laser power to 3.9 mW and made $\theta = 25°$. Figure 6 shows the arrangement used in this comparative study, where it also shows that the spot profile indeed has the shape and dimensions of the tip of the antenna. Therefore, its size could be controlled by changing the cross-section of the tip facing the Air-Bearing surface.

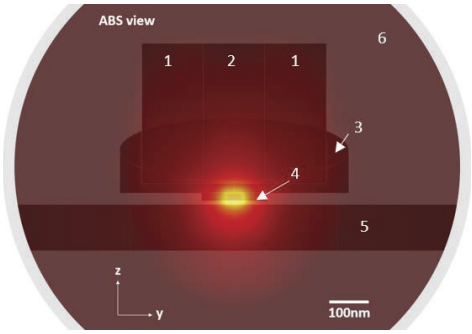

Fig. 6. The figure shows ABS view for the system used in the comparative study presented in Table 2. (1) is the heatsink of the write pole (2), (3) is the elliptical antenna, (4) is the hot spot, (5) is the waveguide, and (6) is the surrounding cladding .

OPTICS CONTINUUM

3. Conclusion

We proposed an optical delivery system for HAMR consisting of an elliptical plasmonic antenna and a V-shaped waveguide design. The dimensions of the elliptical antenna allow tuning the optical and thermal performance of the system. We demonstrated in various examples the ability of the elliptical antenna design to tune the normalised peak temperature metric, which indicates how much laser power is needed to be delivered to the NFT for a specific output; we generated values ranging from ~ 128 K/mW (Fig. 2) to more than 181 K/mW (Table 2, elliptical antenna design (2)).

Such flexibility provides reasonable control to maintain a suitable trade-off between the normalised peak temperature and the thermal efficiency ($\Delta T_{Media}/\Delta T_{NFT}$). In addition, comparative studies with many other NFT designs showed that the thermal gradients in the down-track and the cross-track directions of the recording media produced by the elliptical antenna outperformed those designs. On the other hand, increasing the size of the elliptical NFT will cause the antenna to support higher-order plasmonic modes, which will require considering a new coupling arrangement. Here, the V-shaped waveguide comes into play; its design offers agile coupling between photonic and plasmonic modes by changing the angle between its arms.

Furthermore, as any metallic component such as the write pole near the plasmonic antenna would affect its performance severely, placing the write pole 30 nm above the antenna is challenging. Nevertheless, the tapered antenna, write pole, and the various heatsinks allow dealing with this problem efficiently. It keeps these metallic components far from the bottom surface of the antenna where the plasmonic response occurs, while they are only 30 nm distant above the tip at the front, allowing easy data encoding. Practically, it could also be fabricated inside the gap of the V-shaped waveguide. Such tapered features enhance the thermal performance and offer flexibility in different engineering designs and allow the investigation of complete optical delivery systems for HAMR with the essential metallic components near the NFT.

In general, the proposed system demonstrated tunability and high photonic-plasmonic-thermal conversion efficiency. These results offer multiple pathways for engineering plasmonic NFTs and waveguides to optimise and manage the thermal output in heat-assisted magnetic recording. They also provide important insight for designing effective optical delivery systems for a wide range of other plasmonic applications with different temperature requirements.

Funding. Science Foundation Ireland (12/RC/2278_P2); Engineering and Physical Sciences Research Council (EP/L015323/1).

Acknowledgments. We want to thank the SFI AMBER Research Centre for its support during this work. We would also like to thank the Trinity College High-Performance Center (TCHPC) for its computational support and the use of its facilities. This cluster was funded through grants from the Higher Education Authority through its PRTLI program.

Disclosures. The authors declare no conflicts of interest.

Data availability. No data were generated or analysed in the presented research.

References

1. D. K. Gramotnev and S. I. Bozhevolnyi, "Plasmonics beyond the diffraction limit," Nat. Photonics **4**(2), 83–91 (2010).
2. J. A. Schuller, E. S. Barnard, W. Cai, Y. C. Jun, J. S. White, and M. L. Brongersma, "Plasmonics for extreme light concentration and manipulation," Nat. Mater. **9**(3), 193–204 (2010).
3. G. V. Naik, V. M. Shalaev, and A. Boltasseva, "Alternative plasmonic materials: beyond gold and silver," Adv. Mater. **25**(24), 3264–3294 (2013).
4. W. A. Challener and A. V. Itagi, "Near-field optics for heat-assisted magnetic recording (experiment, theory, and modeling)," in *Modern Aspects of Electrochemistry No. 44*, (Springer, 2009), pp. 53–111.
5. T. Rausch, J. D. Trantham, A. S. Chu, H. Dakroub, J. W. Riddering, C. P. Henry, J. D. Kiely, E. C. Gage, and J. W. Dykes, "Hamr drive performance and integration challenges," IEEE Trans. Magn. **49**(2), 730–733 (2013).
6. M. C. Kautzky and M. G. Blaber, "Materials for heat-assisted magnetic recording heads," MRS Bull. **43**(2), 100–105 (2018).
7. W. A. Challener, C. Peng, A. V. Itagi, D. Karns, W. Peng, Y. Peng, X. Yang, X. Zhu, N. J. Gokemeijer, Y.-T. Hsia, G. Ju, R. E. Rottmayer, M. A. Seigler, and E. C. Gage, "Heat-assisted magnetic recording by a near-field transducer with efficient optical energy transfer," Nat. Photonics **3**(4), 220–224 (2009).

OPTICS CONTINUUM

8. M. Staffaroni, "Circuit analysis in metal-optics, theory and applications," Ph.D. thesis, UC Berkeley (2011).
9. M. H. Kryder, E. C. Gage, T. W. McDaniel, W. A. Challener, R. E. Rottmayer, G. Ju, Y.-T. Hsia, and M. F. Erden, "Heat assisted magnetic recording," Proc. IEEE **96**(11), 1810–1835 (2008).
10. X. Shi, L. Hesselink, and R. L. Thornton, "Ultrahigh light transmission through a c-shaped nanoaperture," Opt. Lett. **28**(15), 1320–1322 (2003).
11. B. C. Stipe, T. C. Strand, C. C. Poon, H. Balamane, T. D. Boone, J. A. Katine, J.-L. Li, V. Rawat, H. Nemoto, A. Hirotsune, O. Hellwig, R. Ruiz, E. Dobisz, D. S. Kercher, N. Robertson, T. R. Albrecht, and B. D. Terris, "Magnetic recording at 1.5 pb m- 2 using an integrated plasmonic antenna," Nat. Photonics **4**(7), 484–488 (2010).
12. E. X. Jin and X. Xu, "Radiation transfer through nanoscale apertures," in *RADIATIVE TRANSFER-IV. Fourth International Symposium on Radiative Transfer*, (Begel House Inc., 2004).
13. R. D. Grober, R. J. Schoelkopf, and D. E. Prober, "Optical antenna: Towards a unity efficiency near-field optical probe," Appl. Phys. Lett. **70**(11), 1354–1356 (1997).
14. K. Şendur and W. Challener, "Near-field radiation of bow-tie antennas and apertures at optical frequencies," J. Microsc. **210**(3), 279–283 (2003).
15. K. Crozier, A. Sundaramurthy, G. Kino, and C. Quate, "Optical antennas: Resonators for local field enhancement," J. Appl. Phys. **94**(7), 4632–4642 (2003).
16. J. Gosciniak, M. Mooney, M. Gubbins, and B. Corbett, "Novel droplet near-field transducer for heat-assisted magnetic recording," Nanophotonics **4**(4), 503–510 (2015).
17. T. Matsumoto, F. Akagi, M. Mochizuki, H. Miyamoto, and B. Stipe, "Integrated head design using a nanobeak antenna for thermally assisted magnetic recording," Opt. Express **20**(17), 18946–18954 (2012).
18. P. D. Dongare, Y. Zhao, D. Renard, J. Yang, O. Neumann, J. Metz, L. Yuan, A. Alabastri, P. Nordlander, and N. J. Halas, "A 3d plasmonic antenna-reactor for nanoscale thermal hotspots and gradients," ACS Nano **15**(5), 8761–8769 (2021).
19. F. Bello, D. Wolf, G. J. Parker, C. Wolf, A. Krichevsky, F. Zong, N. Abadía, and J. F. Donegan, "Optical, thermal, and bit-writing analysis of a directly coupled plasmonic waveguide for heat-assisted magnetic recording," OSA Continuum **3**(8), 2010–2021 (2020).
20. D. Sarid and W. A. Challener, *Modern introduction to surface plasmons: theory, Mathematica modeling, and applications* (Cambridge University Press, 2010).
21. T. Rausch, "Standard media stack and figure of merits for hamr nft modeling," ASTC Heads Working Group, Seagate, Bloomington, MN, USA, Tech. Rep (2011).
22. S. Bhargava, "Heat-assisted magnetic recording: Fundamental limits to inverse electromagnetic design," Ph.D. thesis, UC Berkeley (2015).
23. J. Hlavac, "Melting temperatures of refractory oxides: Part i," Pure Appl. Chem. **54**(3), 681–688 (1982).
24. J. Coutures and M. Rand, "Melting temperatures of refractory oxides-part ii: Lanthanoid sesquioxides," Pure Appl. Chem. **61**(8), 1461–1482 (1989).
25. A. A. Vyshnevyy and D. Y. Fedyanin, "Self-heating and cooling of active plasmonic waveguides," ACS Photonics **3**(1), 51–57 (2016).
26. C. Zhong, P. Flanigan, N. Abadía, F. Bello, B. D. Jennings, G. Atcheson, J. Li, J.-Y. Zheng, J. J. Wang, R. Hobbs, D. McCloskey, and J. F. Donegan, "Effective heat dissipation in an adiabatic near-field transducer for hamr," Opt. Express **26**(15), 18842–18854 (2018).
27. N. Abadía, F. Bello, C. Zhong, P. Flanigan, D. M. McCloskey, C. Wolf, A. Krichevsky, D. Wolf, F. Zong, A. Samani, D. V. Plant, and J. F. Donegan, "Optical and thermal analysis of the light-heat conversion process employing an antenna-based hybrid plasmonic waveguide for hamr," Opt. Express **26**(2), 1752–1765 (2018).
28. C. Multiphysics, "v. 5.2 a. www. comsol. com. comsol ab, stockholm," (2018).
29. L. Miao and T. Y. Hsiang, "Tapered waveguide design for heat-assisted magnetic recording applications," IEEE Trans. Magn. **50**(1), 1–7 (2014).
30. K. P. Lim, V. Krishnamurthy, J. F. Ying, J. Pu, and Q. Wang, "Ultrahigh index and low-loss silicon rich nitride thin film for nir hamr optics," IEEE Trans. Magn. **53**(5), 1–7 (2017).
31. C. Zhong, "Plasmonic waveguides for sub-wavelength light confinement," Trinity College Dublin, the University of Dublin (2018).
32. G. Owen and P. Rissman, "Proximity effect correction for electron beam lithography by equalization of background dose," J. Appl. Phys. **54**(6), 3573–3581 (1983).
33. I. Avrutsky, R. Soref, and W. Buchwald, "Sub-wavelength plasmonic modes in a conductor-gap-dielectric system with a nanoscale gap," Opt. Express **18**(1), 348–363 (2010).
34. N. Abadia, T. Bernadin, P. Chaisakul, S. Olivier, D. Marris-Morini, R. E. de Lamaëstre, J. Weeber, and L. Vivien, "Low-power consumption franz-keldysh effect plasmonic modulator," Opt. Express **22**(9), 11236–11243 (2014).
35. P. Liao and A. Wokaun, "Lightning rod effect in surface enhanced raman scattering," J. Chem. Phys. **76**(1), 751–752 (1982).
36. A. Datta and X. Xu, "Comparative study of optical near-field transducers for heat-assisted magnetic recording," Opt. Eng. **56**(12), 121906 (2017).
37. H. Richter, C. Poon, G. Parker, M. Staffaroni, O. Mosendz, R. Zakai, and B. Stipe, "Direct measurement of the thermal gradient in heat assisted magnetic recording," IEEE Trans. Magn. **49**(10), 5378–5381 (2013).

OPTICS CONTINUUM

38. D. A. Saunders, J. Hohlfeld, X. Zheng, T. Rausch, and C. Rea, "Hamr thermal gradient measurements and analysis," IEEE Trans. Magn. **53**(2), 1–5 (2017).
39. I. Gilbert, D. A. Saunders, P. Czoschke, Z. Liu, S. Granz, and T. Rausch, "Measuring cross-track thermal gradient in heat-assisted magnetic recording," IEEE Trans. Magn. **55**(12), 1–5 (2019).